New insight into photocatalytic CO_2 conversion with nearly 100% CO selectivity by CuO-Pd/H_xMoO_{3-y} hybrids

Haibo Yin, Junhua Li [*]

State Key Joint Laboratory of Environment Simulation and Pollution Control, School of Environment, Tsinghua University, Beijing 100084, PR China

ARTICLE INFO

ABSTRACT

Photocatalytic CO_2 reduction holds promise for solving climate change. However, low conversion efficiency and low product selectivity limit current systems. Here, we report a strategy involving CuO-Pd deposited on H_xMoO_{3-y} with abundant oxygen vacancies (OVs) that drives CO_2 photocatalytic reduction toward CO with nearly 100% selectivity and apparent quantum efficiency of 3.0% at 650 nm in H_2O vapor at 100 °C. Detailed characterizations demonstrate that high performance mainly stems from the synergistic effect of the paired Cu-Pd sites in CuO-Pd and OVs in H_xMoO_{3-y}, where OVs serve as CO_2 adsorption sites and induce the migration of localized electrons across the Schottky barrier to Cu-Pd sites, and then Cu-Pd sites promote CO_2 reduction to CO. Theoretical calculation shows the strong hybridizations of Cu 3d - and Pd 3d - O 2p orbitals accelerate electrons transfer from CuO-Pd to CO_2, effectively optimizing the rate-limiting step ($CO_2 * \rightarrow COOH*$).

1. Introduction

The excessive emission of CO_2 caused by burning fossil fuels has led to worldwide energy and environmental issues [1–6]. In consequence, artificial photosynthetic techniques, mimicking the natural photosynthetic process, for converting CO_2 into carbon-based fuels (such as CO, HCOOH, CH_4, etc.) without damaging the environment have been regarded as an attractive strategy in terms of reducing atmospheric CO_2 [7–11]. Unfortunately, the unsatisfactory performance of current photocatalysts in CO_2 reduction is far below the requirements of practical implementation [11,12]. The main factors for low activity in catalytic system usually involve one or more of the following three points (1) low light absorption capacity; (2) low CO_2 adsorption and activation capacity; and (3) lack of sufficient active sites [13,14]. Thus, various methods, including constructing defect structures, band gap engineering, morphology control, and junction engineering, are proposed to effectively overcome the above-mentioned bottlenecks and obtain high selective products of CO_2 conversion [15–20]. Meanwhile, further raising the reaction temperature of photocatalysis has been deemed as an important strategy to facilitate CO_2 reduction [21–23].

Plasmonic semiconductors with abundant localized electrons induced by plentiful oxygen vacancies (OVs) have been demonstrated to be quite effective in adsorbing and activating CO_2 [24–30]. For example, Ishihara et al. first reported that a large amount of exposed surface OVs

sites on ultrathin plasmonic H_xWO_{3-y} nanotubes can realize stable CO_2 photoreduction to CH_3COOH with a high selectivity > 80% under solar light [24]. As another desirable plasmonic catalyst, H_xMoO_{3-y} has a broad solar light absorption region, which is induced by strong localized surface plasmon resonances (LSPRs) [31–33]. Specifically, upon light irradiation, the surface Mo^{n+} ($4 < n < 6$) species neighboring OVs act as the adsorption and activation sites of CO_2 by abundant localized electrons, indicating the great advantages of OVs in CO_2 conversion [29,34,35].

However, single-component H_xMoO_{3-y} is usually confined by its intrinsic features in heterogeneous photocatalysis [36,37].

CuO-based photocatalysts have attracted extensive attention because Cu species can provide a mass of active sites in CO_2 reduction [38–40]. However, CuO at nanoscale is unstable and consequently generates various byproducts [40,41]. Therefore, we determine to modify CuO by Pd nanoparticles (NPs) to improve the product selectivity in CO_2 reduction [42]. Moreover, the strong binding of H atoms with Pd can suppress the side reaction of H_2 evolution [43]. More importantly, the strategy that inserts Cu atoms into Pd lattice can provide the paired Cu-Pd sites for enhancing CO_2 adsorption and activation, where the side reactions that require adjacent Cu sites are prevented, and subsequent the selectivity of target product is improved [11,43,44].

Herein, we design and fabricate CuO-Pd/H_xMoO_{3-y} hybrids via a solution-processed impregnation-reduction method, where most of Cu

---

atoms are uniformly distributed on Pd NPs in the form of CuO and part of Cu atoms are inserted into Pd lattice in the form of the paired Cu-Pd sites. Thereinto, Cu-Pd sites of CuO-Pd play a more vital role in photocatalytic CO_2 reduction compared to CuO, which act as highly active sites for improving CO selectivity. Based on the synergistic effect of Cu-Pd sites and OVs, CuO-Pd/H_xMoO_{3-y} hybrids achieve nearly 100% CO selectivity with a yield rate of 870 μmol g_{cat}^{-1} h^{-1} under full-spectrum light irradiation at 100 °C. The novel design of CuO-Pd with the paired Cu-Pd sites coupled with OVs certainly improves the selectivity in photocatalytic CO_2 conversion.

2. Experimental section

2.1. Synthesis of CuO-Pd/H_xMoO_{3-y} hybrids

In a typical synthesis, 100 mg of H_xMoO_{3-y} nanosheets was dispersed in 8 mL of an aqueous solution. Then 105 mg of polyvinylpyrrolidone K-30 (PVP), 120 mg of L(+)-Ascorbic acid were added into the glass vial under magnetic stirring in an oil bath present to 80 °C for 10 min. Subsequently, certain amounts of Na_2PdCl_4 and $CuCl_2 2 H_2O$ solutions were injected into the reaction solution where the total content of Cu and Pd remains at 0.2 mmol. The reaction mixture was heated at 80 °C in air for 3 h. The samples were washed with water several times to remove most of PVP and L(+)-Ascorbic acid by centrifugation. The obtained samples were denoted as Cu_1O-Pd_{10}/, Cu_1O-Pd_5/, and Cu_1O-Pd_1/H_xMoO_{3-y}, respectively, according to the amount of added $CuCl_2H_2O$ and Na_2PdCl_4 solutions. Among them, as the catalyst with the best activity in CO production from CO_2 photoreduction, Cu_1O-Pd_5/H_xMoO_{3-y} hybrids are also named CuOPd/H_xMoO_{3-y} hybrids after rigorous and meticulous characterizations. For comparison, CuO/H_xMoO_{3-y} and Pd/H_xMoO_{3-y} were also synthesized in the same manner without the addition of the Na_2PdCl_4 and $CuCl_2 2 H_2O$, respectively.

2.2. Characterization

XRD measurements were recorded using a BRUKER D8/Advance X-ray diffractometer (Cu Kα X-ray: λ = 0.1545 nm). Transmission electron microscopy (TEM) and energy-dispersive spectroscopy (EDS) measurements were performed on a JEOL JEM 2100 microscope with an accelerating voltage of 200 kV. X-ray photoelectron spectroscopy (XPS) and Auger electron spectroscopy measurements were carried out using an ESCALab250XI photoelectron spectrometer. All binding energies were referenced to the C 1 s peak at 284.8 eV. Cu K-edge and Pd K-edge XAFS measurements were performed on the beamline BL01C1 in NSRRC. The radiation was monochromatized by a Si (111) double-crystal monochromator. The isotope labeling experiments were measured by ^1H NMR measurement (Bruker 600-MHz system). UV/Vis-NIR diffuse reflectance spectra were measured on Lambda 900 from PerkinElmer UV WinLab. Photocurrent response, impedance curves, and Mott-Schottky curves were measured by CHI-760E from Shanghai CHENHUA by using platinum foil, and Ag/AgCl (saturated KCl solution) were employed as the counter, and reference electrodes, respectively. ESR spectra were performed on A300–10/12 from Bruker in Germany. PL spectra (EX WL: 200 – 450 nm) and time-resolved fluorescence decay spectra were measured by FLS1000/FSS from Edinburgh, UK. In situ diffuse reflectance infrared Fourier transform spectroscopy was measured on NEXUS, 870 FT-IR.

2.3. Determination of apparent quantum efficiency (AQE)

Under different monochromatic light wavelengths (350, 365, 420, 475, 550, 650, 765, and 800 nm) irradiation, the values of light intensities are measured to 1.27, 1.36, 2.82, 3.58, 3.28, 3.65, 3.71, and 3.95 mW.cm^{-2} corresponding to the 350, 365, 420, 475, 550, 650, 765, and 800 nm incident wavelength, respectively. The apparent quantum efficiency (AQE) was measured. The CO yields are measured after 1 h

photocatalytic reaction, and the AQE is calculated on the basis of the following equation:

$$AQE = \frac{\text{Number of reacted electrons}}{\text{Number of incident photons}} = \frac{\text{Number of generated CO} \times 2}{\text{Number of incident photons}}$$
$$= \frac{M * N_A * 2}{\frac{I \times A \times t}{hv}}$$

Where M represents the amount of CO generation, N_A represents Avogadro's constant, I is the light intensity, A is the light incident area (4 cm^2), t is light irradiation time, h and v are Planck constant and the incident light frequency, respectively. *2.4. Photocatalytic CO_2 Conversion measurement.*

The photocatalytic CO_2 reduction measurement was conducted by homemade photocatalytic reactor (Fig. S12). The total volume of the reactor was about 200 mL. In the reactor, a small quartz beaker had a height of 2 cm and a diameter of 2 cm, where the photocatalysts (10 mg of CuO-Pd/H_xMoO_{3-y} or reference samples) were laid out. A 300 W Xe lamp was used as the light source and positioned is 5 cm above the reactor. The catalytic reaction was typically performed for 1 h after bubbling with CO_2 gas and H_2O vapor for 30 min at various temperatures. The CO was converted to CH_4 by a methanation reactor and then analyzed by the FID. The isotopic-labeled experiments were performed using $^{13}CO_2$ instead of $^{12}CO_2$, and the products were analyzed using gas chromatography-mass spectrometry (GC-MS, 7890 A and 5975 C, Agilent).

2.4. DFT calculation detail

The Vienna ab initio simulation package (VASP, version 5.4.4) was utilized to calculate the properties of catalysts. All the model structures were optimized by using the Perdew-BurkeErnzerhof (PBE) form of the generalized gradient approximation plus the Hubbard model (GGA+U), with a 400 eV of kinetic cutoff energy. A [3 × 3] supercell and four Pd, Cu, and Pd-Cu (111) atomic layers was used for the plane-wave expansion of the electronic wave function, respectively, of which two bottom layers were fixed to their bulk positions during the geometry optimizations. Thereinto, the atomic ratio of Cu to Pd was close to that of ICP-OES results. The slab models of the support H_xMoO_{3-y} (010) for above nanoparticles were constructed. These slab models were separated by a 15 Å vacuum combined with a 3 × 3 × 1 Gamma-Pack k-point mesh due to the large crystal cell (~18 Å × 18 Å) of slab model. Moreover, all slab models were relaxed until the SCF tolerance was below 10^{-6} eV and atomic forces were below 0.05 eV/Å.

3. Results and discussion

3.1. Structure and morphology

CuO-Pd/H_xMoO_{3-y} hybrids are synthesized by solvothermal method and subsequent solutionprocessed impregnation-reduction method (Fig. S1a) similarly to the protocol for PdCu-TiO_2 hybrids structures [43]. CuO-Pd with a face-centered cubic (fcc) phase are in situ grown on plasmonic H_xMoO_{3-y} nanosheets, where the atomic ratios of Pd to Cu can be controlled by adjusting the concentrations of Pd and Cu precursors. Fig. 1a-b display the transmission electron microscopy (TEM) images of Cu_1O-Pd_{10}/H_xMoO_{3-y} and Cu_1O-Pd_5/H_xMoO_{3-y} (or named CuO-Pd/H_xMoO_{3-y}). Obvious aggregations of CuO-Pd (white circles) are found in Cu_1OPd_{10}/H_xMoO_{3-y} hybrids. In addition, Cu_1O-Pd_{10}/H_xMoO_{3-y} also shows another three shapes of sphere (yellow circles), cubic (red squares), and rod (blue triangles), in which sphere (Fig. S2) and rod (Fig. S3) should be ascribed to CuO-Pd and cubic represents the Pd NPs (Fig. S4). On the contrary, for CuO-Pd/H_xMoO_{3-y} hybrids obtained by increasing the content of Cu, CuO-Pd has only comparable sphere shapes with a mean size of 4.5 nm, completely different from the cubic structures of Pd NPs with mean size
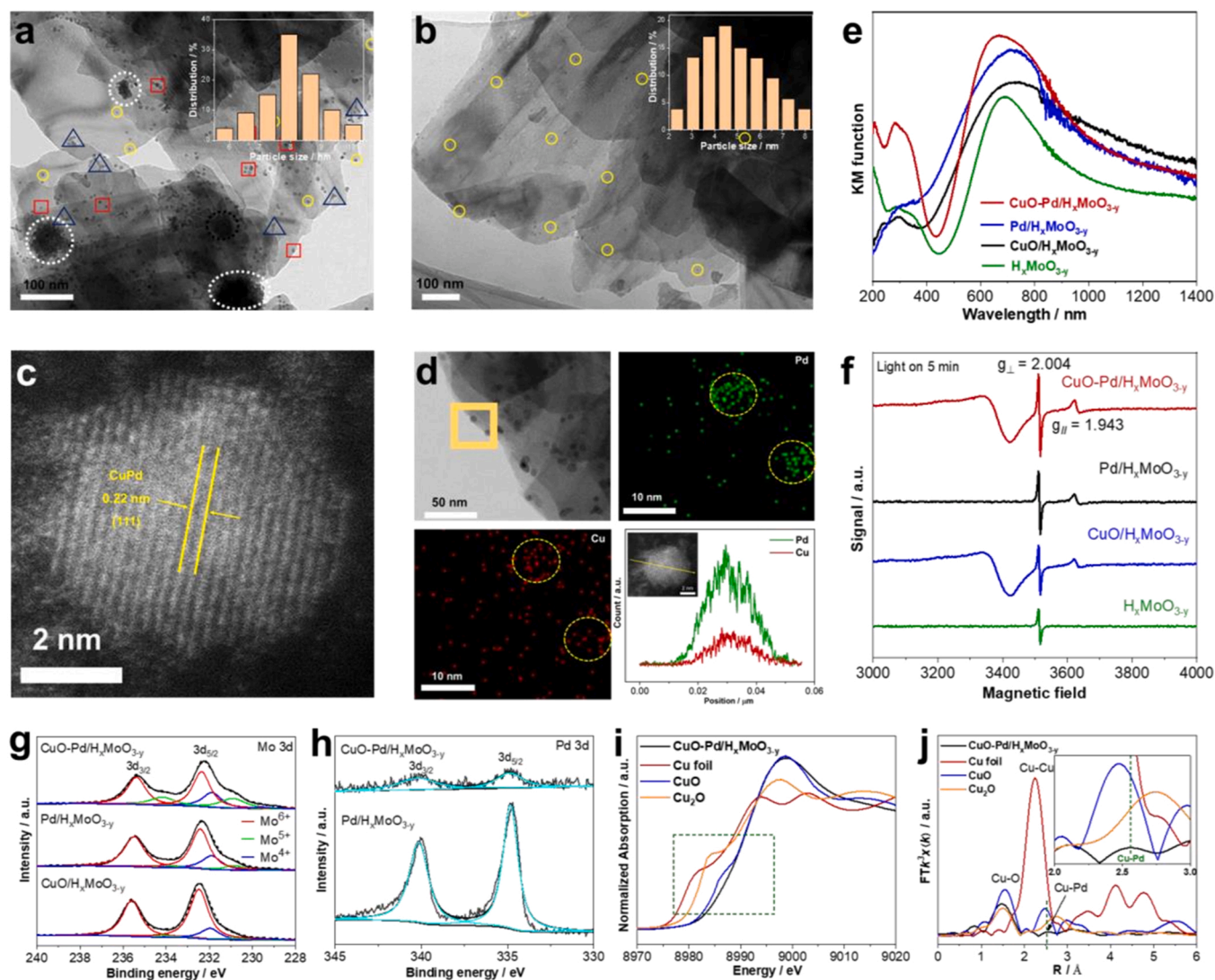
Fig. 1. a) TEM images of Cu_1O-Pd_{10}/H_xMoO_{3-y} (inset, particle size distribution of CuO-Pd sphere) and b) CuO-Pd/H_xMoO_{3-y} hybrids (inset, particle size distribution of CuO-Pd). c) HAADFSTEM image of CuO-Pd/H_xMoO_{3-y} hybrids. d) TEM image and corresponding EDS elemental mapping images of CuO-Pd/H_xMoO_{3-y}. e) UV-Vis-NIR diffuse reflectance spectra and f) ESR spectra of CuO-Pd/H_xMoO_{3-y} hybrids and references samples. g) Mo 3d and h) Pd 3d XPS spectra of CuO-Pd/H_xMoO_{3-y} hybrids and reference samples, respectively. i) Cu K-edge XANES spectra and j) FT-EXAFS spectra of CuO-Pd/H_xMoO_{3-y}, Cu foil, Cu_2O, and CuO, respectively.

of 10 nm in Pd/H_xMoO_{3-y} (Fig. S4b). Atomic-resolution high-angle annular dark-field scanning transmission electron microscope (HAADF-STEM) image (Fig. 1c) displays that CuO-Pd has the lattice spacing of 0.22 nm, which corresponds to the (111) plane of fcc Pd NPs. The more Cu atoms are embedded, the more lattice spacing of Pd NPs decreases (Fig. S5). Meanwhile, energy dispersive spectroscopy (EDS) mapping technique and the corresponding EDS elemental line scan are performed to reveal the spatial distribution of Cu and Pd elements (Fig. 1d), almost the same locations of Cu and Pd species confirm the uniform distribution of CuO on Pd NPs. Furthermore, according to UV/Vis-NIR diffuse reflectance spectra (Fig. 1e), CuO-Pd/H_xMoO_{3-y} hybrids show prominent symmetrical LSPR peak induced by OVs at 670 nm. Similarly, H_xMoO_{3-y}, Pd/H_xMoO_{3-y}, and CuO/H_xMoO_{3-y} hybrids also exhibit LSPR peaks but with slightly weaker absorption intensity, indicating relatively low OVs content. Electron spin resonance (ESR) spectra can resolve the unpaired electrons left by the existence of oxygen vacancies (Fig. 1f). ESR spectrum of CuO-Pd/H_xMoO_{3-y} shows a hyperfine structure with perpendicular ($g_{\bigcirc} = 2.004$) and parallel ($g_{\parallel} = 1.943$) bands. Therein, g value at 1.943 suggests the existence of Mo-O tetragonal pyramids. And the signal at g value (2.004) corresponding to typical five-coordinated Mo^{5+} is for the free electrons, underlining

that electrons mainly locate in OVs around Mo^{5+} atoms rather than delocalize over CuO-Pd. Notably, the ESR intensity of CuOPd/H_xMoO_{3-y} is stronger than that of H_xMoO_{3-y}, CuO/H_xMoO_{3-y}, and Pd/H_xMoO_{3-y}, demonstrating that more free electrons exist in CuO-Pd/H_xMoO_{3-y}. The orthorhombic phase (JCPDS No.5–0508) of H_xMoO_{3-y} in CuO-Pd/H_xMoO_{3-y} hybrids is confirmed by X-ray diffraction (XRD, Fig. S6b), which is crystallized in a layered structure composed of MoO_6 octahedra by sharing edges and corners (Fig. S6c). Moreover, we employ inductively coupled plasma-optical emission spectroscopy (ICP-OES) to analyze the molar ratios of Cu to Pd. As listed in Table S1, we obtain a series of samples (Cu_1O-Pd_1/, Cu_1O-Pd_5/, and Cu_1O-Pd_{10}/H_xMoO_{3-y}) with various atomic ratios of Cu to Pd and comparable total molar contents of Cu and Pd (11–13%). X-ray photoelectron spectroscopy (XPS) measurements were performed to elucidate the oxidation states of Mo, Pd, and Cu elements. Unlike H_xMoO_{3-y} (Fig. S1c), it is evident that not only Mo^{6+} and Mo^{5+} but also Mo^{4+} species exist in CuO-Pd/H_xMoO_{3-y} hybrids (Fig. 1g). Furthermore, based on XPS peak areas of Mo 3d, Mo^{6+}, Mo^{5+}, and Mo^{4+} cations account for 42.0%, 23.9%, and 34.1% of the total Mo element, respectively. The average oxidation state of Mo is thus calculated to be 5.08, which mainly arises from the oxygen vacancies. Compared to

CuO-Pd/H_xMoO_{3-y} hybrids, the total proportion of Mo^{5+} and Mo^{4+} cations in Pd/H_xMoO_{3-y} (42.4%) and CuO/H_xMoO_{3-y} (36.1%) has decreased significantly, corresponding to their intensity of light absorption. Given Pd 3d XPS spectra of CuO-Pd/H_xMoO_{3-y} hybrids (Fig. 1h), two peaks with binding energies at 334.8 and 340.2 eV are attributed to the $3d_{5/2}$ and $3d_{3/2}$ peaks of Pd^0, respectively. Two peaks at 932.5 eV (Cu $2p_{3/2}$) and 952.6 eV (Cu $2p_{1/2}$) and the miscellaneous peaks in the red rectangle of Cu 2p are ascribed to Cu^{2+} in CuO-Pd/H_xMoO_{3-y} hybrids (Fig. S7). By adjusting the molar ratio of Pd and Cu, the oxidation states (Fig. S8) and optical property (Fig. S9) of the obtained Cu_1O-Pd_{10}/H_xMoO_{3-y} and Cu_1O-Pd_1/H_xMoO_{3-y} hybrids are consistent with that of Cu_1Pd_5/H_xMoO_{3-y} hybrids.

3.2. Structural parameters and coordination environment

X-ray absorption fine structure (XAFS) measurements can further precisely resolve the local structural information of Cu and Pd atoms, where normalized X-ray absorption near-edge structure (XANES) spectra and Fourier transformation of k^3-weighted normalized extended XAFS (FTEXAFS) spectra are given. According to previous reports [43, 45], based on the similar Cu K-edge spectra shape with CuO, the valence state of Cu species in CuO-Pd/H_xMoO_{3-y} is attributed to Cu^{2+} corresponding to XPS analysis (Fig. S7). The only difference is that the disappearing absorption peak (green rectangle) in CuO-Pd/H_xMoO_{3-y} fits the characteristics of Pd K-edge spectra (Fig. 1i and Fig. S10a), suggesting some Cu atoms are embedded into Pd lattice. Meanwhile, the peak at 2.6 Å of CuO-Pd/H_xMoO_{3-y} fits the characteristics to Pd-Pd bond (2.6 Å) rather than CuCu bond (2.3 Å), revealing these embedded Cu atoms are coordinated with Pd atoms (Cu-Pd bond) in Pd lattice (Fig. 1j and Fig. S10b) [43]. In addition, the strong peak at 1.5 Å (Cu-O bond) suggests that most Cu species in CuO-Pd/H_xMoO_{3-y} hybrids exist primarily as CuO. On the contrary, Pd K-edge spectra of CuO-Pd/H_xMoO_{3-y} have no apparent difference from that of Pd foil, indicating the original Pd lattice remains intact even when some Cu atoms are inserted. Wavelet transform X-ray absorption fine structure (WT-EXAFS) is performed to correlate the FT-EXAFS peaks with K and R spaces (Fig. S11a-d). The WT intensity at 1.5 Å (black rectangle) of CuOPd/H_xMoO_{3-y} hybrids apparently corresponds to that of CuO.
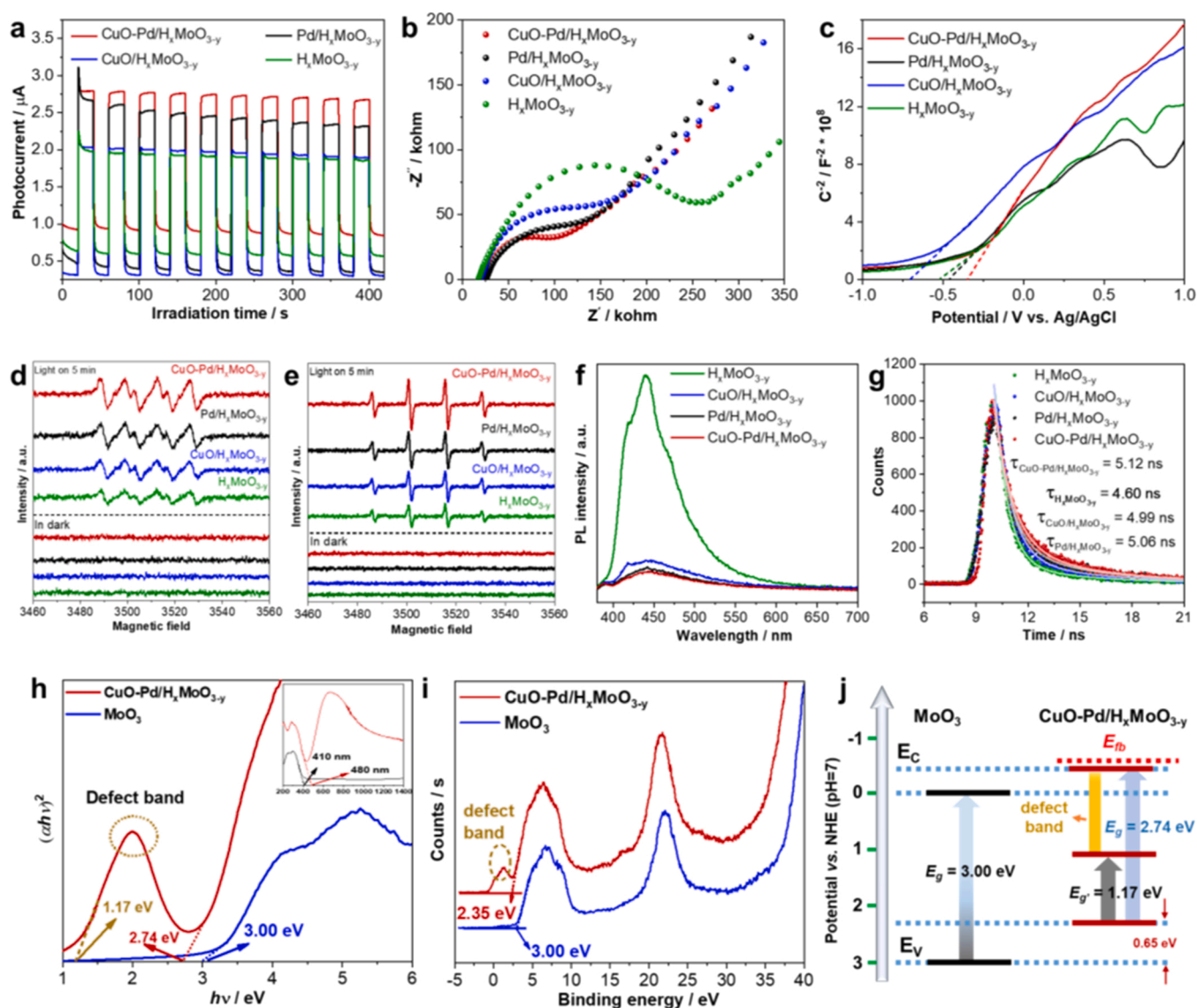

Fig. 2. a) Transient photocurrent responses, b) electrochemical impedance spectra (EIS), c) Mott-Schottky curves under light irradiation, d) $O_2^{\bullet-}$ (trapped by DMPO in methanol), e) $^\bullet$OH radical (trapped by DMPO in water), f) PL spectra, g) time-resolved fluorescence decay spectra of CuO-Pd/H_xMoO_{3-y}, Pd/H_xMoO_{3-y}, CuO/H_xMoO_{3-y}, and H_xMoO_{3-y}. h) Tauc plots deduced from UV/Vis absorption spectra (Inset), i) XPS valence band spectra, and j) electronic band structure of CuO-Pd/H_xMoO_{3-y} hybrids and MoO_3.

Meanwhile, the weaker WT intensity at 3.2 Å (yellow rectangle) should be attributed to the Cu-Pd coordination. To better extract the quantitative chemical configuration of Cu and Pd atoms, EXAFS fitting is conducted to obtain the Cu and Pd coordination environment (Fig. S11e-h). Based on these fitting results, most Cu species exist in the main form $Cu-O_2$ coordination and a small number of Cu atoms are coordinated to three Pd atoms ($Cu-Pd_3$) (Table S2). Based on the above detailed characterizations, we successfully synthesized $CuO-Pd/H_xMoO_{3-y}$ hybrids where most of Cu atoms are uniformly distributed on Pd NPs in the form of CuO and part of Cu atoms are inserted into Pd lattice in the form of Cu-Pd sites.

3.3. Photo-electric characterization of $CuO-Pd/H_xMoO_{3-y}$

The separation efficiencies of the photogenerated electron-hole on $CuO-Pd/H_xMoO_{3-y}$ hybrids and references were studied by photocurrent measurements (Fig. 2a). Apparently, the addition of CuO-Pd and Pd NPs dramatically improves the photocurrent of H_xMoO_{3-y}, indicating Pd-based cocatalysts are more conducive to promoting charge separation. Meanwhile, the current density of $CuO-Pd/H_xMoO_{3-y}$ is obviously higher than that of Pd/H_xMoO_{3-y}, which suggests that CuO-Pd can construct more effective Schottky junction with H_xMoO_{3-y} to enhance separation efficiency of photoexcited electron-hole pairs. The electrochemical impedance spectra indicate that $CuOPd/H_xMoO_{3-y}$ hybrids have a higher electronic conductivity, which is mainly attributed to the more efficient electron transfer across the interface of CuO-Pd and H_xMoO_{3-y} (Fig. 2b). Then, we use the Mott-Schottky spectra for analyzing the flat band potential (E_{fb}) under light irradiation (Fig. 2c). The E_{fb} values calculated from the intercept of the axis with potential values are -0.36, -0.46, -0.70, and -0.52 V vs Ag/AgCl for $CuO-Pd/H_xMoO_{3-y}$, Pd/H_xMoO_{3-y}, CuO/H_xMoO_{3-y}, and H_xMoO_{3-y}, respectively. Compared to reference samples, the E_{fb} potential of $CuO-Pd/H_xMoO_{3-y}$ shifts to positive potential, leading to a lower surface work function. The smaller the work function is, the more easily electrons transfer from H_xMoO_{3-y} to CuO-Pd [46]. ESR measurements were further performed to detect the radical species $O_2^{\bullet-}$ (Fig. 2d) and $^{\bullet}OH$ (Fig. 2e) by using 5,5dimethyl-1-pyrroline N-oxide (DMPO) as spin-trapping agents. All photocatalysts show no signal in dark conditions while they can generate $O_2^{\bullet-}$ and $^{\bullet}OH$ under light irradiation. Thereinto, $CuOPd/H_xMoO_{3-y}$ hybrids have the strongest ability to generate $O_2^{\bullet-}$ and $^{\bullet}OH$, indicating the key role of CuO-Pd in producing radical species by photoelectrons. Meanwhile, photoluminescence (PL) spectroscopy (Fig. 2f) was employed to study the interface-related dynamics of charge carriers, where the peak at 450 nm can be attributed to radiative recombination of photogenerated charge.

The PL intensity follows the order of $CuO-Pd/H_xMoO_{3-y} < Pd/H_xMoO_{3-y} < CuO/H_xMoO_{3-y} < H_xMoO_{3-y}$, highlighting that CuO-Pd can better improve the charge-separation efficiency across interface. Furthermore, in ns-level time-resolved fluorescence spectra (Fig. 2g), $CuOPd/H_xMoO_{3-y}$ hybrids have the longest delay time among the all photocatalysts in PL decay curves, further suggesting that the photogenerated electrons of H_xMoO_{3-y} are more easily transferred to CuO-Pd instead of recombining with the holes. Before performing the CO_2 reduction reaction, we further determine the band structure positions of $CuO-Pd/H_xMoO_{3-y}$ hybrids in light of the above advantages of CuO-Pd. The absorption edge of $CuO-Pd/H_xMoO_{3-y}$ hybrids exhibits a clear red shift from 410 to 480 nm relative to that of MoO_3 (Fig. 2h, inset). Moreover, the bandgap value of $CuO-Pd/H_xMoO_{3-y}$ hybrids (2.74 eV) that is calculated by the plots of $(ahv)^2$ against (hv) has 0.26 eV less than that of MoO_3 (3.0 eV), implying $CuO-Pd/H_xMoO_{3-y}$ hybrids can be more easily excited by light irradiation. Notably, the bandgap is further shrunk from 2.74 to 1.17 eV ($E_{g'}$) with the assistance of the OVs-induced defect band (DB), which has proven to be an important factor in improving photocatalytic performance [46]. According to the valence band XPS (VB-XPS) spectra (Fig. 2i), the valence bands of MoO_3 and $CuO-Pd/H_xMoO_{3-y}$ hybrids are 3.00 and 2.35 eV, respectively.

Evidently, the defect band induces a sublevel in VB spectra of $CuO-Pd/H_xMoO_{3y}$ hybrids, which derives from the localized electrons in d-orbitals of low-valence Mo^{5+} ions. By the analysis above, we make the diagram of the band energy of $CuO-Pd/H_xMoO_{3-y}$ hybrids and MoO_3 (Fig. 2j). Different from MoO_3, the conduction band of $CuO-Pd/H_xMoO_{3-y}$ hybrids is much lower than E_{fb} due to the contribution of the emerging defect band, which is the character of degenerate semiconductors [26]. Through the meticulous analysis of photocarriers migration and electronic band structure, we can conclude that CuO-Pd is conducive to reducing the bandgap of H_xMoO_{3-y}, making it easier to be excited under light irradiation, and the resulting photogenerated electrons are rapidly transferred to the surface of CuO-Pd through the formed Schottky barrier, thereby performing CO_2 reduction.

3.4. Photocatalytic CO_2 reduction performance of $CuO-Pd/H_xMoO_{3-y}$

Upon acquiring the fine structures, we are now in a position to investigate the efficacy of CuOPd coupled with defective H_xMoO_{3-y} in the enhancement of photocatalytic CO_2 reduction by our homemade reactor (Fig. S12), where a 300 W Xe lamp is used as the light source and positioned is 5 cm above the reactor. Based on the high selectivity of CO and the high total yield of CO and CH_4, we carefully optimized the molar ratio of Cu and Pd (Fig. S13) and the temperature of CO_2 reduction (Fig. S14), and finally selected Cu_1O-Pd_5 and 100 °C as the optimal ratio and reduction temperature. Fig. 3a shows the average production rate of CO/CH_4 in photocatalytic CO_2 reduction with H_2O vapor at 25 °C ($CO_2 + 2 H^+ + 2e^- \rightarrow CO + H_2O$) by various H_xMoO_{3-y}-based samples. Compared with H_xMoO_{3-y}, the load of CuO or Pd NPs can improve CO yield rates but not significantly. The CO yield rate of $CuO-Pd/H_xMoO_{3-y}$ hybrids significantly enhances compared to that of H_xMoO_{3-y}, CuO/H_xMoO_{3-y}, and Pd/H_xMoO_{3-y}. Considering that light absorption has no obvious variation after loading CuO, Pd, or CuO-Pd on H_xMoO_{3-y} (Fig. 1e), this activity improvement should be attributed primarily to the formed Cu-Pd sites, which can effectively promote charge seperation and CO_2 activation [43]. Fig. 3b shows the yield rates of CO/CH_4 in the thermocatalytic CO_2 reduction at 100 °C. H_xMoO_{3-x} exhibits negligible activity while $CuO-Pd/H_xMoO_{3-y}$, CuO/H_xMoO_{3-y}, and Pd/H_xMoO_{3-y} hybrids also show weak performance, which should be related to the deficient photogenerated electron as well as the rapid desorption of CO_2 at high temperatures. In addition, all catalysts are incapable of producing CH_4 under photocatalysis alone and thermocatalysis alone. Notably, in photocatalytic CO_2 reduction system at 100 °C (Fig. 3c), the performances of all catalysts have been greatly improved. Thereinto, the CO yield of $CuO-Pd/H_xMoO_{3-y}$ achieves 870 μmol g_{cat}^{-1} h^{-1}, which is 26.4, 10.4, 4.6 times higher than that of H_xMoO_{3-y}, CuO/H_xMoO_{3-y}, Pd/H_xMoO_{3-y}, respectively, highlighting the key role of the formed Cu-Pd sites. This CO yield rate is also 20.9 and 116 times as high as that in photocatalysis and thermocatalysis condition, respectively, indicating that there is a significant synergistic effect of light and heat. That is, heat can accelerate the migration of photogenerated electrons to CuO-Pd and directly activate the Cu-Pd active sites for promoting photocataytic CO_2 reduction. In turn, $CuO-Pd/H_xMoO_{3-y}$ hybrids can absorb the photon energy by full-spectrum irradiation and quickly convert it into thermal energy, which cause a high surface temperature, leading the generated heat promptly transfers to the surrounding Cu-Pd sites of CuO-Pd [47]. Moreover, this photocatalytic performance of $CuO-Pd/H_xMoO_{3-y}$ hybrids is much better than the catalysts reported in literature (Table S3). Meanwhile, the yield rate of CH_4 by $CuO-Pd/H_xMoO_{3y}$ hybrids only accounts for 0.8% of the sum of CH_4 and CO, indicating the high selectivity of 99.2% for CO production. On the other hand, to investigate the contribution of LSPRs on the catalytic activity of $CuO-Pd/H_xMoO_{3-y}$ hybrids and reference samples, full-spectrum, visible light ($\lambda > 420$ nm), and visible light with a longer wavelength ($\lambda > 600$ nm) were studied (Fig. 3d). Under three light conditions, there is no significant difference in the activities for $CuO-Pd/H_xMoO_{3-y}$ hybrids. H_xMoO_{3-y}, CuO/H_xMoO_{3-y}, and Pd/H_xMoO_{3-y} hybrids also show
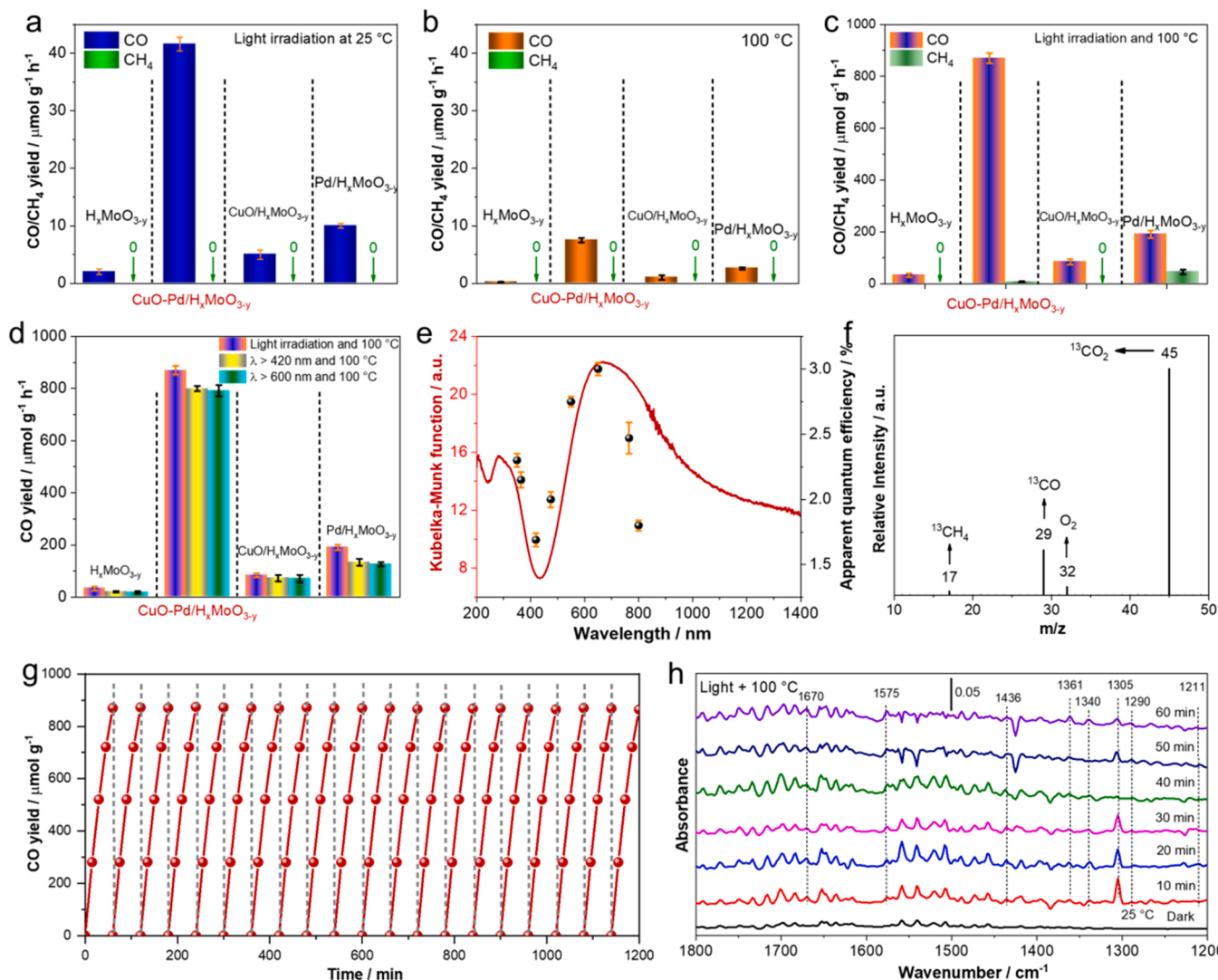
Fig. 3. Average yield rates of CO and CH$_4$ in a) photocatalytic CO$_2$ reduction under fullspectrum light irradiation at 25 °C, b) thermocatalytic CO$_2$ reduction at 100 °C, and c) photocatalytic CO$_2$ reduction under full-spectrum at 100 °C with H$_2$O vapor over CuOPd/H$_x$MoO$_{3-y}$ hybrids and references. d) CO yield rate under different wavelengths at 100 °C with H$_2$O vapor. e) Calculated AQEs (black dots) for CO$_2$ reduction at 100 °C with H$_2$O vapor under monochromatic light irradiation, in reference to its UV-Vis-NIR diffuse reflectance spectra. f) Mass spectra of ^{13}CO ($m/z = 29$) and ^{13}CH$_4$ ($m/z = 17$) produced in photocatalytic ^{13}CO$_2$ reduction at 100 °C. g) Photocatalytic stability of CuO-Pd/H$_x$MoO$_{3-y}$ hybrids for CO$_2$ reduction, where the used catalysts are reduced in H$_2$ atmosphere at 100 °C to recover OVs before performing the next experiment. h) In situ DRIFT spectra of CuO-Pd/H$_x$MoO$_{3-y}$ hybrids after ambient temperature adsorption of CO$_2$ under full-spectrum irradiation at 100 °C.

similar phenomenon, thus confirming photoelectrons generated by H$_x$MoO$_{3-y}$ come not from the band-gap excitation, but from the contribution of plasmonic effect of H$_x$MoO$_{3-y}$. This conclusion is further verified by using various monochromatic light (Fig. 3e), where the apparent quantum efficiencies (AQEs) of CuO-Pd/H$_x$MoO$_{3-y}$ hybrids are calculated by the amount of generated CO. The AQEs well match the light absorption and achieve the maximum (3.0%) at λ = 650 nm, further emphasizing that the trigger point of high activity stems from the LSPR effect of H$_x$MoO$_{3-y}$. Taken together, the high CO selectivity of CuO-Pd/H$_x$MoO$_{3-y}$ hybrids in photocatalytic CO$_2$ reduction at 100 °C is mainly attributed to two synergies: (1) the synergistic effect of CuO-Pd (Cu-Pd sites, to be more precise) and OVs; (2) the synergistic effect between light and heat.

In addition, to verify the origins of CO and CH$_4$, we have traced the carbon sources in the reactions using a ^{13}C isotopic label. Fig. 3f shows the mass spectra of CO and CH$_4$ products using ^{13}CO$_2$ as substrate under identical photocatalytic catalytic reaction conditions. The peaks at *m/z* = 17 and m/z = 29 can be assigned to ^{13}CH$_4$ and ^{13}CO, demonstrating

that the carbon source of CH$_4$ and CO indeed stem from the used CO$_2$. Furthermore, the photocatalytic stability of CuOPd/H$_x$MoO$_{3-y}$ hybrids was assessed (Fig. 3g). CO production is well-maintained within 1200 min and the structure, chemical oxidation state, and optical stability of hybrids still retain after cyclic tests (Fig. S15), indicating the potential application of CuO-Pd/H$_x$MoO$_{3-y}$ hybrids.

3.5. Photocatalytic mechanism analysis

To further investigate the origin of high CO selectivity of CuO-Pd/H$_x$MoO$_{3-y}$ hybrids on photocatalytic CO$_2$ reduction, an in situ diffuse reflectance Fourier transform infrared spectroscopy (DRIFT) study was performed (Fig. 3h and Fig. S16), which is a powerful technique to look into the reaction intermediates and mechanism. Firstly, the homemade reactor is vacuumized for 60 min and then filled by CO$_2$ at 25 °C without incident light and heat. To exclude environment factors, the baselines are deducted from all spectra. In the presence of incident light and heat (100 °C) (Fig. 3h), the spectra for the exposure of CuO-Pd/H$_x$MoO$_{3-y}$

hybrids to CO_2 exhibit some significant differences in the range of 1200–1800 cm^{-1}, whereas these changes in the incident light or heat alone are significantly weaker. Therein, the peak at 1340 cm^{-1} is ascribed to the formation of carbonate-like (CO_3^-) species, which is in good agreement with the reported values [41]. The d(OH) bending and symmetric stretching of surface bicarbonate HCO_3 * species correspond to the vibrational peaks at 1211 and 1436 cm^{-1}, which stems from the CO_2 adsorption. As the most crucial intermediates during the formation of CO_2 to CO under photocatalytic condition, the characteristic peaks of the COOH* are found at 1290, 1361, and 1575 cm^{-1}. Notably, the broadened peak at 1305 cm^{-1} is assigned to the CO* adsorption, implying the formation of CO and CH_4. Meanwhile, with the increase of reaction time, the intensity of this peak gradually weakens. This is mainly because H_xMoO_{3-y} is oxidized by the generated O_2, thus

reducing the amount of OVs and further leading to the decrease of light absorbance. In addition, the signals located at 3014 and 3033 cm^{-1} belong to the C-O stretching vibrations of CO* . According to the DRIFT analysis, we can deduce that the CuO-Pd dramatically improve the generation of HCO_3, CO* , CO_3^-, and HCOOH* species, which is the key role in photocatalytic CO_2 reduction to CO. On the contrary, in the range of 1200–1800 cm^{-1} of the spectra, the quite weak signals for incident light (Fig. S16a) or heat (Fig. S16b) conditions indicate that CO are hard to detect in gas phase or at catalyst surface, which well matches their inferior performance in CO_2 conversion.

3.6. DFT calculations

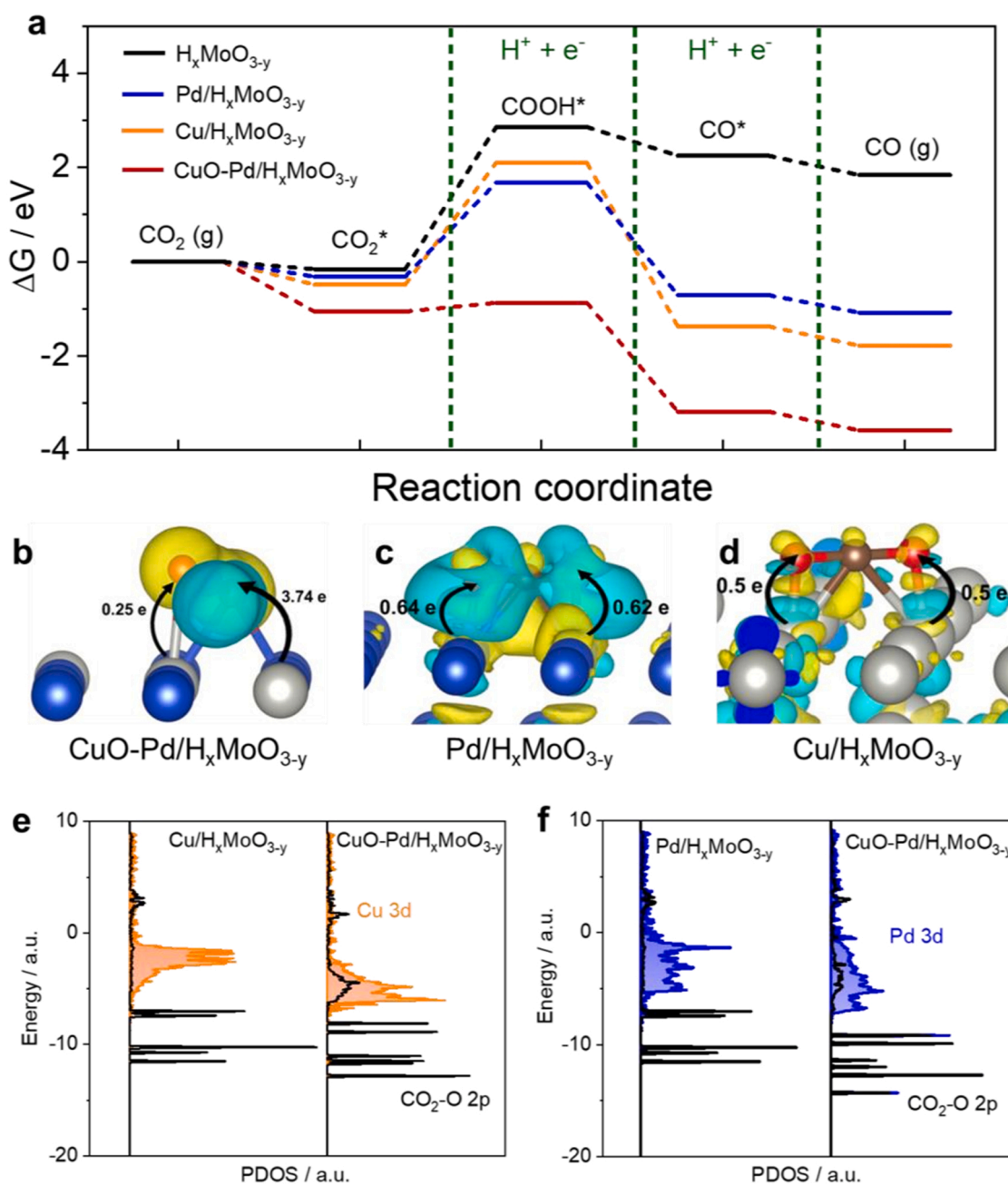Based on the analysis of DRIFT and the key role of the paired Cu-Pd

Fig. 4. a) The minimum energy pathway that results in CO product. Charge density difference and corresponding charge transfer on b) CuO-Pd/H_xMoO_{3-y}, c) Pd/H_xMoO_{3-y}, and d) Cu/H_xMoO_{3-y}. e) Projected density of states (PDOS) plots of CuO-Pd/H_xMoO_{3-y} and Cu/H_xMoO_{3-y}. f) Projected density of states (PDOS) plots of CuO-Pd/H_xMoO_{3-y} and Pd/H_xMoO_{3-y}.

sites of CuO-Pd in photocatalytic CO_2 reduction, the relative free energies (ΔG) on the intermediates in reduction process of CO_2 * to CO* are detected over CuO-Pd/H_xMoO_{3-y} hybrids and reference samples (Fig. 4a). As an important step for the whole reaction process, the initial adsorption of CO_2 molecules shows a marked difference by comparing different photocatalysts. Four photocatalysts are capable of spontaneously adsorbing CO_2 due to the existence of oxygen vacancies. Meanwhile, CuO-Pd/H_xMoO_{3-y} hybrids have a stronger CO_2 adsorption capacity owing to the lower free energy (−1.05 eV) than that of Pd/H_xMoO_{3-y} (−0.32 eV), Cu/H_xMoO_{3-y} (−0.48 eV), and H_xMoO_{3-y} (−0.16 eV). Notably, for the rate-determining step, CO_2 * → COOH*, the energy barrier on CuOPd/H_xMoO_{3-y} hybrids is 0.18 eV, which is obviously lower than that of Pd/H_xMoO_{3-y} (2.0 eV), Cu/H_xMoO_{3-y} (2.59 eV), and H_xMoO_{3-y} (3.02 eV). Moreover, this value is also far below the energy barrier (3.35 eV) of the rate-determining step of CH_4 (Fig. S17), which accounts for the high selectivity of CO. The above result suggests that the formation of COOH* intermediate on CuO-Pd/H_xMoO_{3-y} hybrids is kinetically more favorable than that of reference catalysts and CO_2 activation can proceed more smoother with the assistance of the paired Cu-Pd sites. Based on the subsequent steps (COOH* + H^+ + e^- → CO* + H_2O and CO* → CO (g)), the yield of CO over CuO-Pd/H_xMoO_{3-y} hybrids will spontaneously occur. To further probe the mechanism, the charge density differences of CuO-Pd/H_xMoO_{3-y} hybrids-CO_2 *, Cu/H_xMoO_{3-y}-CO_2 *, and Pd/$H_xMoO_{3-y}CO_2$ * are calculated (Fig. 4b-d). Apparently, for CuO-Pd/H_xMoO_{3-y} hybrids, the electron clouds are strongly localized around Pd-O-C-O-Cu active site (in which the yellow area represents the electrons enrichment while the light blue represents electrons deficiency). In addition, according to the Bader charge in CO_2 adsorption state, the number of electrons transfer from Pd (3.74e) and Cu (0.25e) of CuO-Pd/H_xMoO_{3-y} hybrids to CO_2 * -O is much more than that from Cu (1.0e) of Cu/H_xMoO_{3-y} and Pd (1.26e) of Pd/H_xMoO_{3-y}, suggesting that CO_2 * -O coordinated Cu and Pd of CuO-Pd have stronger covalent character. Specifically, the photoelectrons generated from plasmonic H_xMoO_{3-y} under photocatalytic condition will transfer to Cu and Pd atoms in CuOPd/H_xMoO_{3-y}. Subsequently, using the paired Cu-Pd sites of CuO-Pd as springboards, electrons can easily be transferred to the coordinated O of CO_2 * by Pd-O-C-O-Cu bonds. In addition, the electronic band structure between Cu-Pd active sites and adsorbed CO_2 * is further clarified by the projected density of states (PDOS) among the 3*d* orbitals of Cu and Pd of Cu-Pd sites in CuOPd/H_xMoO_{3-y} and the 2*p* orbits of CO_2-O (Fig. 4e-f). By comparing to the overlap between the Cu 3*d* - O 2*p* and Pd 3*d* - O 2*p*, the *p-d* orbital hybridizations between Cu or Pd atoms of the paired Cu-Pd sites in CuO-Pd/H_xMoO_{3-y} and O atoms in CO_2 are obviously stronger than that of both Cu/H_xMoO_{3-y} and Pd/H_xMoO_{3-y}. This can effectively form the strong chemical bonds of Cu-O and Pd-O and subsequent facilitates the electrons transfer from Cu and Pd of the paired Cu-Pd sites to CO_2.

4. Conclusion

In this work, we report a strategy to reduce CO_2 for obtaining high activity in photocatalysis by depositing CuO-Pd on H_xMoO_{3-y} with abundant OVs. This performance is realized by constructing the synergistic effect of the paired Cu-Pd sites in CuO-Pd and OVs in H_xMoO_{3-y} coupled with the synergetic effect of light and heat. That is, OVs can effectively induce the transfer of localized electrons to CuO-Pd across Schottky junctions, and Cu-Pd sites of CuO-Pd further promote CO_2 activation and reduction under photocatalytic condition, finally obtaining the CO selectively of nearly 100% and AQE of 3.0% at 650 nm in H_2O vapor at 100 °C. This work puts forward a new idea to give deep insight into the mechanism of CO_2 conversion by developing high performance Cu-based composites/plasmonic semiconductors.

CRediT authorship contribution statement

Haibo Yin and Junhua Li proposed and designed experiments. Haibo Yin performed the experiments and analyzed data. All authors discussed, commented on and revised the manuscript.

Declaration of Competing Interest

The authors declare that they have no known competing financial interests or personal relationships that could have appeared to influence the work reported in this paper.

Data Availability

Data will be made available on request.

Appendix A. Supporting information

Supplementary data associated with this article can be found in the online version at doi:10.1016/j.apcatb.2022.121927.

References

[1] H.A. Wilcox, W.J. North, CO_2 reduction and reforestation, Science 242 (1988) 1493–1494.

[2] A.W. Fairhall, Accumulation of Fossil CO_2 in the atmosphere and the sea, Nature 245 (1973) 20–23.

[3] T.M.L. Wigley, P.D. Jones, P.M. Kelly, Scenario for a warm, High-CO_2 world, Nature 283 (1980) 17–21.

[4] T.M.L. Wigley, P.D. Jones, Detecting CO_2-induced climatic change, Nature 292 (1981), 205208.

[5] T. Zheng, M. Zhang, L. Wu, S. Guo, X. Liu, J. Zhao, W. Xue, J. Li, C. Liu, X. Li, Q. Jiang, J. Bao, J. Zeng, T. Yu, C. Xia, Upcycling CO_2 into energy-rich long-chain compounds via electrochemical and metabolic engineering, Nat. Catal. 5 (2022) 388–396.

[6] S.X. Ren, D. Joulie, D. Salvatore, K. Torbensen, M. Wang, M. Robert, C. P. Berlinguette, Molecular electrocatalysts can mediate fast, selective CO_2 Reduction in a flow cell, Science 365 (2019) 367–369.

[7] Y. Wang, S.B. Wang, S.L. Zhang, X.W. Lou, Formation of hierarchical $FeCoS_2$-$CoS2$ doubleshelled nanotubes with enhanced performance for photocatalytic reduction of CO_2, Angew. Chem. Int. Ed. 59 (2020) 11918–11922.

[8] H.N. Huang, R. Shi, Z.H. Li, J.Q. Zhao, C.L. Su, T.R. Zhang, Triphase photocatalytic CO_2 reduction over silver-decorated titanium oxide at a gas-water boundary, Angew. Chem. Int. Ed. 61 (2022), e202200802.

[9] Y.J. Ma, X.X. Yi, S.L. Wang, T. Li, B.E. Tan, C.C. Chen, T. Majima, E.R. Waclawik, H.Y. Zhu, J.Y. Wang, Selective photocatalytic CO_2 reduction in aerobic environment by microporous Pd-porphyrin-based polymers coated hollow TiO_2, Nat. Commun. 13 (2022) 1400.

[10] K.Y. Niu, Y. Xu, H.C. Wang, R. Ye, H.L. Xin, F. Lin, C.X. Tian, Y.W. Lum, K. C. Bustillo, M.M. Doeff, M.T.M. Koper, J. Ager, R. Xu, H.M. Zheng, A spongy nickel-organic CO_2 reduction photocatalyst for nearly 100% selective CO production, Sci. Adv. 3 (2017), 17009211700929.

[11] G. Wang, C.T. He, R. Huang, J.J. Mao, D.S. Wang, Y.D. Li, Photoinduction of Cu single atoms decorated on UiO-66-NH_2 for enhanced photocatalytic reduction of CO_2 to liquid fuels, J. Am. Chem. Soc. 142 (2020) 19339–19345.

[12] H. Rao, L.C.S. Chmidt, J. Bonin, M. Robert, Visible-light-driven methane formation from CO_2 with a molecular iron catalyst, Nature 548 (2017) 74–77.

[13] X.C. Jiao, Z.W. Chen, X.D. Li, Y.F. Sun, S. Gao, W.S. Yan, C.M. Wang, Q. Zhang, Y. Lin, Y. Luo, Y. Xie, Defect-mediated electron-hole separation in one-unit-cell $ZnIn_2S_4$ layers for boosted solar-driven CO_2 reduction, J. Am. Chem. Soc. 139 (2017) 7586–7594.

[14] Y.X. Pan, Y. You, S. Xin, Y.T. Li, G.T. Fu, Z.M. Cui, Y.L. Men, F.F. Cao, S.H. Yu, J. B. Goodenough, Photocatalytic CO_2 reduction by carbon-coated indium-oxide nanobelts, J. Am. Chem. Soc. 139 (2017) 4123–4129.

[15] Y. Chen, G. Jia, Y.F. Hu, G.Z. Fan, Y.H. Tsang, Z.S. Li, Z.G. Zou, Two-dimensional nanomaterials for photocatalytic CO_2 reduction to solar fuels, Sustain. Energy Fuels 1 (2017) 1875–1898.

[16] J.L. White, M.F. Baruch, J.E. Pander, Y. Hu, I.C. Fortmeyer, J.E. Park, T. Zhang, K. Liao, J. Gu, Y. Yan, T.W. Shaw, E. Abelev, A.B. Bocarsly, Light-driven heterogeneous reduction of carbon dioxide: photocatalysts and photoelectrodes, Chem. Rev. 115 (2015) 12888–12935.

[17] S.Z. Xu, E.A. Carter, Theoretical insights into heterogeneous (photo) electrochemical CO_2 reduction, Chem. Rev. 119 (2019) 6631–6669.

[18] X. Chang, T. Wang, J. Gong, CO_2 photo-reduction: insights into CO_2 activation and reaction on surfaces of photocatalysts, Energy Environ. Sci. 9 (2016) 2177–2196.

[19] P. Zhang, S. Wang, B.Y. Guan, X.W. Lou, Fabrication of CdS hierarchical multi-cavity hollow particles for efficient visible light CO_2 reduction, Energy Environ. Sci. 12 (2019), 164168.

[20] A. Dhakshinamoorthy, S. Navalon, A. Corma, H. Garcia, Photocatalytic CO_2 reduction by TiO_2 and related titanium containing solids, Energy Environ. Sci. 5 (2012) 9217–9233.

[21] Z.Y. Wu, C.R. Li, Z. Li, K. Feng, M.J. Cai, D.K. Zhang, S.H. Wang, M.Y. Chu, C. C. Zhang, J.H. Shen, Z. Huang, Y.L. Xiao, G.A. Ozin, X.H. Zhang, L. He, Niobium and titanium carbides (MXenes) as superior photothermal supports for CO_2 photocatalysis, ACS Nano 15 (2021), 56965705.

[22] J.C. Zhu, W.W. Shao, X.D. Li, X.C. Jiao, J.F. Zhu, Y.F. Sun, Y. Xie, Asymmetric TripleAtom sites confined in ternary oxide enabling selective CO_2 photothermal reduction to acetate, J. Am. Chem. Soc. 143 (2021) 18233–18241.

[23] Y.H. Qi, L.Z. Song, S.X. Ouyang, X.C. Liang, S.B. Ning, Q.Q. Zhang, J.H. Ye, Photoinduced defect engineering: enhanced photothermal catalytic performance of 2D Black In_2O_{3-x} nanosheets with bifunctional oxygen vacancies, Adv. Mater. 32 (2020), 1903915.

[24] S.M. Sun, M. Watanabe, J. Wu, Q. An, T. Ishihara, Ultrathin WO_3 center dot 0.33H (2)O nanotubes for CO_2 photoreduction to acetate with high selectivity, J. Am. Chem. Soc. 140 (2018) 6474–6482.

[25] G. Prusty, J.T. Lee, S. Seifert, B.B. Muhoberac, R. Sardar, Ultrathin plasmonic tungsten oxide quantum wells with controllable free carrier densities, J. Am. Chem. Soc. 142 (2020) 5938–5942.

[26] I. Kriegel, F. Scotognella, L. Manna, Plasmonic doped semiconductor nanocrystals: properties, fabrication, applications and perspectives, Phys. Rep. 674 (2017) 1–52.

[27] X.Y. Wu, Y. Li, G.K. Zhang, H. Chen, J. Li, K. Wang, Y. Pan, Y. Zhao, Y.F. Sun, Y. Xie, Photocatalytic CO_2 conversion of $M_{0.33}WO_3$ directly from the air with high selectivity: insight into full spectrum-induced reaction mechanism, J. Am. Chem. Soc. 141 (2019) 5267–5274.

[28] X.P. Zhang, F.W. Tang, M. Wang, W.B. Zhan, H.X. Hu, Y.R. Li, R.H. Friend, X. Y. Song, Femtosecond visualization of oxygen vacancies in metal oxides, Sci. Adv. 6 (2020) eaax9427.

[29] H. Xin, L. Lin, R.T. Li, D. Li, T.Y. Song, R.T. Mu, Q. Fu, X.H. Bao, Overturning CO(2) hydrogenation selectivity with high activity via reaction-induced strong metal-support interactions, J. Am. Chem. Soc. 144 (2022) 4874–4882.

[30] H. Li, F. Qin, Z.P. Yang, X.M. Cui, J.F. Wang, L.Z. Zhang, New reaction pathway induced by plasmon for selective benzyl alcohol oxidation on BiOCl possessing oxygen vacancies, J. Am. Chem. Soc. 139 (2017) 3513–3521.

[31] H.B. Yin, Z. Chen, Y. Peng, S.C. Xiong, Y.D. Li, H. Yamashita, J.H. Li, Dual active centers bridged by oxygen vacancies of ruthenium single-atom hybrids supported on molybdenum oxide for photocatalytic ammonia synthesis, Angew. Chem. Int. Ed. 61 (2022), e202114242.

[32] A. Wold, W. Kunnmann, A. Ferretti, R.J. Arnott, Preparation + properties of sodium + potassium molybdenum bronze crystals, Inorg. Chem. 3 (1964) 545–547.

[33] H.F. Cheng, M.C. Wen, X.C. Ma, Y. Kuwahara, K. Mori, Y. Dai, B.B. Huang, H. Yamashita, Hydrogen doped metal oxide semiconductors with exceptional and tunable localized surface plasmon resonances, J. Am. Chem. Soc. 138 (2016) 9316–9324.

[34] H. Ge, Y. Kuwahara, K. Kusu, H. Yamashita, Plasmon-induced catalytic CO_2 hydrogenation by a nano-sheet Pt/H_xMoO_{3-y} hybrid with abundant surface oxygen vacancies, J. Mater. Chem. A 9 (2021) 13898–13907.

[35] Y. Kuwahara, T. Mihogi, K. Hamahara, K. Kusu, H. Kobayashi, H. Yamashita, A QuasiStable molybdenum sub-oxide with abundant oxygen vacancies that promotes CO_2 hydrogenation to methanol, Chem. Sci. 12 (2021) 9902–9915.

[36] H.F. Cheng, X.F. Qian, Y. Kuwahara, K. Mori, H. Yamashita, A. Plasmonic, Molybdenum oxide hybrid with reversible tunability for visible-light-enhanced catalytic reactions, Adv. Mater. 27 (2015) 4616–4621.

[37] Y. Kuwahara, Y. Yoshimura, K. Haematsu, H. Yamashita, Mild deoxygenation of sulfoxides over plasmonic molybdenum oxide hybrid with dramatic activity enhancement under visible light, J. Am. Chem. Soc. 140 (2018) 9203–9210.

[38] P.Q. Li, J.F. Xu, H. Jing, C.X. Wu, H. Peng, J. Lu, H.Z. Yin, Wedged N-doped CuO with more negative conductive band and lower overpotential for high efficiency photoelectric converting CO_2 to methanol, Appl. Catal. B 156 (2014) 134–140.

[39] S.I. In, D.D. Vaughn, R.E. Schaak, Hybrid $CuO-TiO_{2-x}N_x$ hollow nanocubes for photocatalytic conversion of CO_2 into methane under solar irradiation, Angew. Chem. Int. Ed. 51 (2012) 3915–3918.

[40] M. Wen, B.B. Ren, X.Z. Ye, J.X. He, H. Jiang, C.R. Xiong, Hierarchical loading of CuO on SiO_2 aerogel@High crystalline TiO_2 nanofibers for efficiently photocatalytic reduction of CO_2 without sacrificial agent, Nano Res. 15 (2022) 3872–3879.

[41] S. Neatu, J.A. Macia-Agullo, P. Concepcion, H. Garcia, Gold-copper nanoalloys supported on TiO_2 as photocatalysts for CO_2 reduction by water, J. Am. Chem. Soc. 136 (2014), 1596915976.

[42] G. Kyriakou, M.B. Boucher, A.D. Jewell, E.A. Lewis, T.J. Lawton, A.E. Baber, H. L. Tierney, M. Flytzani-Stephanopoulos, E.C.H. Sykes, Isolated metal atom geometries as a strategy for selective heterogeneous hydrogenations, Science 335 (2012) 1209–1212.

[43] R. Long, Y. Li, Y. Liu, S.M. Chen, X.S. Zheng, C. Gao, C.H. He, N.S. Chen, Z.M. Qi, L. Song, J. Jiang, J.F. Zhu, Y.J. Xiong, Isolation of Cu atoms in Pd lattice: forming highly selective sites for photocatalytic conversion of CO_2 to CH_4, J. Am. Chem. Soc. 139 (2017) 4486–4492.

[44] K. Zhao, X.W. Nie, H.Z. Wang, S. Chen, X. Quan, H.T. Yu, W.Y. Choi, G.H. Zhang, B. Kim, J.G.G. Chen, Selective electroreduction of CO_2 to acetone by single copper atoms anchored on N-doped porous carbon, Nat. Commun. 11 (2020) 2455.

[45] K.A. Goulas, S. Sreekumar, Y. Song, P. Kharidehal, G. Gunbas, P.J. Dietrich, G. R. Johnson, Y.C. Wang, A.M. Grippo, L.C. Grabow, A.A. Gokhale, F.D. Toste, Synergistic effects in bimetallic palladium-copper catalysts improve selectivity in oxygenate coupling reactions, J. Am. Chem. Soc. 138 (2016) 6805–6812.

[46] N. Zhang, A. Jalil, D.X. Wu, S.M. Chen, Y.F. Liu, C. Gao, W. Ye, Z.M. Qi, H.X. Ju, C. M. Wang, X.J. Wu, L. Song, J.F. Zhu, Y.J. Xiong, Refining defect states in $W_{18}O_{49}$ by Mo doping: a strategy for tuning N_2 activation towards solar-driven nitrogen fixation, J. Am. Chem. Soc. 140 (2018) 9434–9443.

[47] H. Song, J. Ye, Photothermal tandem catalysis for CO_2 hydrogenation to methanol, Chem 8 (2022) 1181–1183.